



Decoding Bilateral Hindlimb Kinematics From Cat Spinal Signals Using Three-Dimensional Convolutional Neural Network

Yaser Fathi¹ and Abbas Erfanian^{1,2*}

¹ Department of Biomedical Engineering, School of Electrical Engineering, Iran Neural Technology Research Centre, Iran University of Science and Technology, Tehran, Iran, ² School of Cognitive Sciences, Institute for Research in Fundamental Sciences (IPM), Tehran, Iran

OPEN ACCESS

Edited by:

Mesut Sahin,
New Jersey Institute of Technology,
United States

Reviewed by:

Samit Chakrabarty,
University of Leeds, United Kingdom
Alain Frigon,
Université de Sherbrooke, Canada

*Correspondence:

Abbas Erfanian
erfanian@iust.ac.ir

Specialty section:

This article was submitted to
Neuroprosthetics,
a section of the journal
Frontiers in Neuroscience

Received: 25 October 2021

Accepted: 02 March 2022

Published: 25 March 2022

Citation:

Fathi Y and Erfanian A (2022)
Decoding Bilateral Hindlimb
Kinematics From Cat Spinal Signals
Using Three-Dimensional
Convolutional Neural Network.
Front. Neurosci. 16:801818.
doi: 10.3389/fnins.2022.801818

To date, decoding limb kinematic information mostly relies on neural signals recorded from the peripheral nerve, dorsal root ganglia (DRG), ventral roots, spinal cord gray matter, and the sensorimotor cortex. In the current study, we demonstrated that the neural signals recorded from the lateral and dorsal columns within the spinal cord have the potential to decode hindlimb kinematics during locomotion. Experiments were conducted using intact cats. The cats were trained to walk on a moving belt in a hindlimb-only condition, while their forelimbs were kept on the front body of the treadmill. The bilateral hindlimb joint angles were decoded using local field potential signals recorded using a microelectrode array implanted in the dorsal and lateral columns of both the left and right sides of the cat spinal cord. The results show that contralateral hindlimb kinematics can be decoded as accurately as ipsilateral kinematics. Interestingly, hindlimb kinematics of both legs can be accurately decoded from the lateral columns within one side of the spinal cord during hindlimb-only locomotion. The results indicated that there was no significant difference between the decoding performances obtained using neural signals recorded from the dorsal and lateral columns. The results of the time-frequency analysis show that event-related synchronization (ERS) and event-related desynchronization (ERD) patterns in all frequency bands could reveal the dynamics of the neural signals during movement. The onset and offset of the movement can be clearly identified by the ERD/ERS patterns. The results of the mutual information (MI) analysis showed that the theta frequency band contained significantly more limb kinematics information than the other frequency bands. Moreover, the theta power increased with a higher locomotion speed.

Keywords: neural decoding, spinal cord, locomotion, descending tracts, ascending tracts, convolutional neural network

INTRODUCTION

Neural interfaces have the potential to restore limb function by translating neural activities into command signals that could be used in a neuroprosthetic device for people with spinal cord injury (SCI) (Jackson and Zimmermann, 2012). Restoring the lost function, such as locomotion, requires the integration of both motor and sensory information. Sensory information is an essential

requirement for the closed-loop control of locomotion. Many attempts have been made to obtain sensory information from different parts of the nervous system, such as the peripheral nerve (Riso et al., 2000; Micera et al., 2001; Hansen et al., 2004; Song et al., 2017), dorsal root ganglia (DRG) (Stein et al., 2004; Weber et al., 2006, 2007; Rigosa et al., 2011; Wagenaar et al., 2011; Bruns et al., 2013; Holinski et al., 2013; Han et al., 2017; Kashkoush et al., 2019), ventral roots (Debnath et al., 2014), and spinal cord gray matter (Yeganegi et al., 2018; Fathi and Erfanian, 2019). Moreover, intracortical recordings were used to decode the hindlimb kinematics and muscle electromyographs (EMGs) during bipedal walking in monkeys (Fitzsimmons et al., 2009) and rats (Rigosa et al., 2015) and during quadrupedal locomotion in rats (Song et al., 2009; Barroso et al., 2019). These studies suggest that cortical recording can be used to bypass spinal cord injuries. Several studies have examined the intracortical regulation of the spinal circuit through epidural electrical stimulation (Capogrosso et al., 2016; Knudsen and Moxon, 2017; Bonizzato et al., 2018).

Another possible source of hindlimb kinematic information is the descending pathways (i.e., motor tracts). Motor signals are sent from the brain to the spinal cord through descending tracts. The main descending pathways, including the corticospinal and rubrospinal tracts, play a significant role in controlling balance, posture, locomotion, and reaching. Reticulospinal pathways are also critical in initiating locomotion, postural control, and postural muscle tone. The rubrospinal and corticospinal tracts together with the medullary reticulospinal tract project all to the lateral columns in spinal cord (Lemon, 2008; Rossignol et al., 2009; Frigon et al., 2011; Takakusaki et al., 2016). The previous studies revealed that there was a correlation between the neural signals recorded from the descending tracts and forelimb movements (Prasad and Sahin, 2006, 2010, 2012; Guo et al., 2014). Recently, it was demonstrated that the EMG signals of the forelimb flexor and extensor can be decoded from the lateral columns (Guo et al., 2018; Gok and Sahin, 2019).

In the previous study, we decoded the kinematics of only one leg using the neural signals recorded from the lateral and dorsal columns on one side of the spinal cord during cat hindlimb-only locomotion (Fathi and Erfanian, 2021). A linear regression model was used for decoding hindlimb joint angles. In the current study, we expanded the previous work and decoded the kinematics of both hindlimbs from neural activity recorded from the descending lateral tracts and from the ascending tracts during voluntary hindlimb-only walking on the treadmill. Moreover, we demonstrated that the neural signals recorded from the spinal cord could reflect the speed of locomotion.

Another critical issue in decoding kinematic information from neural signals is the decoding model. Different decoding methods have been employed for this purpose. Linear regression methods were used to estimate the hindlimb kinematics from populations of neurons in the DRG (Stein et al., 2004; Weber et al., 2006, 2007; Bruns et al., 2013; Holinski et al., 2013). To improve the performance of decoding limb kinematics, different nonlinear methods, including particle filtering (Wagenaar et al., 2011), fuzzy neural network (FNN) model (Rigosa et al., 2011), and recurrent neural networks (RNNs) (Han et al., 2017; Yeganegi

et al., 2018) have also been employed. It was demonstrated that the nonlinear model provided better decoding accuracy than the multiple linear regression and Kalman filter estimators (Han et al., 2017). Recently, we proposed a probabilistic recurrent neural network (PRNN) for decoding hindlimb kinematics from neural activity recorded from the dorsal horn of the spinal cord. We demonstrated the superiority of the PRNN over the conventional recurrent neural network and Kalman filter (Fathi and Erfanian, 2019).

In contrast to the previous work, in which a linear regression model was used for decoding, in the current study, a three-dimensional convolutional neural network (3D-CNN) was employed for decoding kinematic information. In recent years, tremendous interest in CNNs has emerged as the most established deep learning algorithm. CNN is a biologically inspired model that can learn high-level local features by convolving a set of filters with input data (LeCun et al., 2015; Patterson and Gibson, 2017). CNNs have achieved significant progress in image processing (Li et al., 2021), video (Liu et al., 2020), speech (Mustaqeem and Kwon, 2020), and natural language processing (Widiastuti, 2019; Li et al., 2020). CNNs have also been applied extensively in cortical signal processing for different applications (Zhang et al., 2021) such as brain-computer interfaces (Lawhern et al., 2018; Craik et al., 2019; Kundu and Ari, 2020; Zhang et al., 2021) decoding finger kinematics (Xie et al., 2018; Petrosyan et al., 2021) and seizure detection (Gao et al., 2020). Recently, it was shown that CNN outperformed linear decoder in estimating EMG signals from neural signals recorded from the spinal cord (Guo et al., 2018). In the current study, we used a 3D-CNN with a regression layer to decode the hindlimb joint kinematics from neural signals recorded from the lateral column as well as from the dorsal column. We also compared the performance of the 3D-CNN with conventional decoding models such as partial least squares (PLS) (Geladi and Kowalski, 1986) and Lasso (Zou and Hastie, 2005).

MATERIALS AND METHODS

The animals used in this study were kept and handled in compliance with the Experimental Animal Regulation Ordinances defined by the Ministry of Health and Medical Education, IRAN. All surgical procedures and experimental protocols involving animal models described in this paper were approved by the Institutional Animal Care and Ethics Committee of the Iran Neural Technology Research Center, Iran University of Science and Technology. All protocols and methods were performed according to the recommendations and relevant guidelines for the care and use of laboratory animals.

Microwire Array Fabrication

Neural signals were recorded from the spinal cord using a custom-made microelectrode array. The array was fabricated using PFA-insulated tungsten wires with a diameter of 50 μm (No. 795500, A-M Systems, United States). As depicted in **Figure 1**, eight microwires were arranged in two rows with an inter-electrode spacing of ~ 1.5 mm in each row to cover the

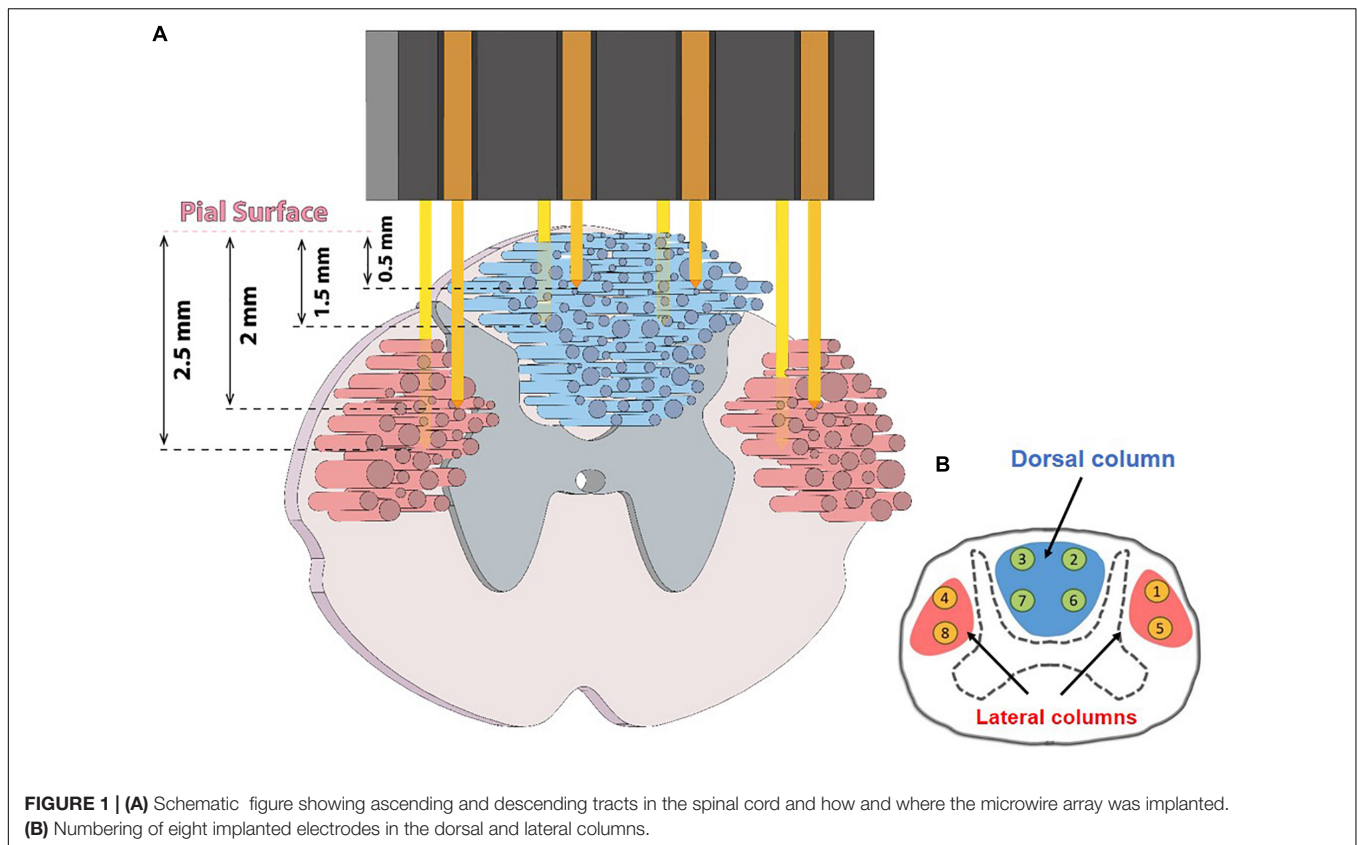


FIGURE 1 | (A) Schematic figure showing ascending and descending tracts in the spinal cord and how and where the microwire array was implanted. **(B)** Numbering of eight implanted electrodes in the dorsal and lateral columns.

distance from left to right lateral columns. In each row, the length of the microwires that should be inserted in the lateral columns of the spinal cord were considered longer than those that should be inserted in the dorsal column of the spinal cord (~ 0.5 – 1.5 mm length for the dorsal column electrodes and 1.5 – 2.5 mm for the lateral column). The lengths of the microwires of the second row were considered to be about ~ 0.5 mm longer than the first row to cover different depths.

Implantation Process

The experiments were conducted on two male cats (3.1–4.2 kg). Prior to surgery, the cats were trained for approximately 2 months to walk on the treadmill. We encouraged the animals to walk by rewarding with the pellet food. Initial anesthesia was induced by intramuscular injection of ketamine (20 mg/kg) into the cranial thigh muscle. The animals were then intubated with endotracheal tube and maintained at a surgical level of anesthesia under isoflurane inhalation (1.0–3.0% in O_2). A partial 4×4 mm laminectomy was performed over the left (with respect to the rostral-caudal vector) L4 vertebra. Four screws were inserted into the bone of the L4 vertebra in the bulkier regions. We utilized these screws as anchors for the array and connector. The array and connector were fixed to the vertebra using dental acrylic.

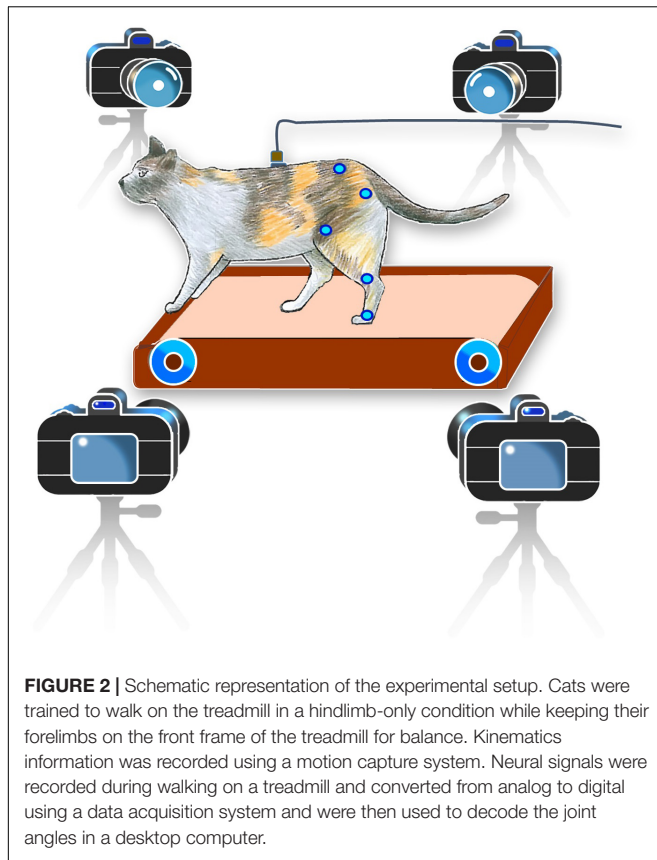
The animal was then placed on a stereotactic frame (SN-1N, Narishige Group Product, Japan). The electrode array connector was attached to a micromanipulator (SM-15, Narishige Group Product, Japan) that could control the three-dimensional

positioning of the electrode with a minimum graduation of $10 \mu\text{m}$. To implant the electrode, a 4×4 mm section of the dura mater below the L4 vertebra was gently opened with an iridectomy scissor to obtain direct access to the spinal cord. Then, the array was vertically inserted into the target position in the spinal cord to cover the dorsal column and both the left and right lateral columns (Figure 1). After implantation, the surface of the spinal cord was covered with a thin layer of Sylgard 184. Then, the array and connector were attached to the bone using metal screws and dental acrylic. The DC and LC, at the L3–L4 spinal segments, typically cover a span of 0.0 – 1.5 and 1.5 – 3.0 mm laterally from the midline to the lateral side and a span of 0.0 – 1.5 and 1.5 – 3.0 mm in depth from the dorsal surface, respectively. The microelectrode array was implanted in the range 0.5 – 2.5 mm laterally from the midline and 0.5 – 2.5 mm in depth from the dorsal surface to cover the DC and LC. A tungsten reference wire was placed proximally in the epidural space of the spinal canal.

After surgery, necessary care, such as regular injection of Cefazolin and tramadol were taken to reduce the risk of infection and to relieve pain. Cefazolin (30 mg/kg) was intramuscularly injected twice daily for a week and tramadol (2 mg/kg) daily for 2 or 3 days after surgery. The urination and excretion of the animals were monitored daily to check for possible abnormalities.

Data Collection

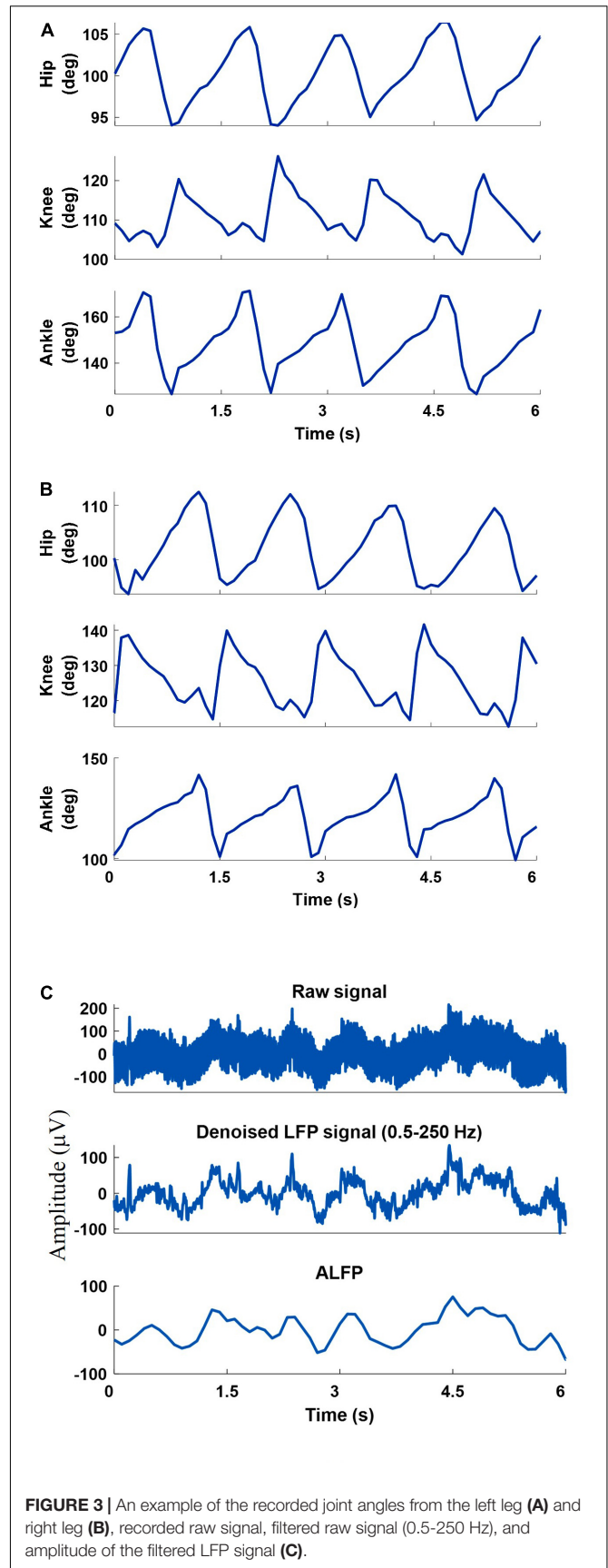
The neural signal and kinematics of the hindlimbs were collected almost once a week. On each experimental day, one to three



recording sessions were conducted. In cat 1, 18 sessions of the experiment were conducted for 14 weeks and in cat 2, 10 sessions were conducted. The duration of each recording session was 2–3 min. On average, each cat took 40 steps per minute. During each session, the animals could walk on a running treadmill with their hindlimbs only while keeping their forelimbs on the front frame of the treadmill (Figure 2). It should be noted that locomotor pattern resulted during hindlimb-only locomotion with placing forelimbs on a stationary platform is different from that resulted during normal quadrupedal locomotion (Harnie et al., 2022). The walking cadence of cat 1 varied between 0.59 and 0.8 steps per second, while the walking cadence of cat 2 had less variation between 0.9 and 0.99 steps per second.

Joint Angle Measurements

A 6-camera motion capture system (Vicon Motion Systems Ltd., United Kingdom) was used to measure the joint angles at a sampling rate of 50 Hz. To measure the hindlimb joint angles of both legs, ten reflective markers were attached to the iliac crest, greater trochanter (hip joint), lateral condyle of the femur (knee joint), lateral malleolus (ankle joint), and the distal end of the fifth metatarsophalangeal joints of both legs. Three-dimensional positions of markers were obtained using a motion capture software (Tracker 2.2, Vicon, United Kingdom). Using the measured positions of the five markers of each leg, three joint angles (ankle, knee, and hip) were calculated



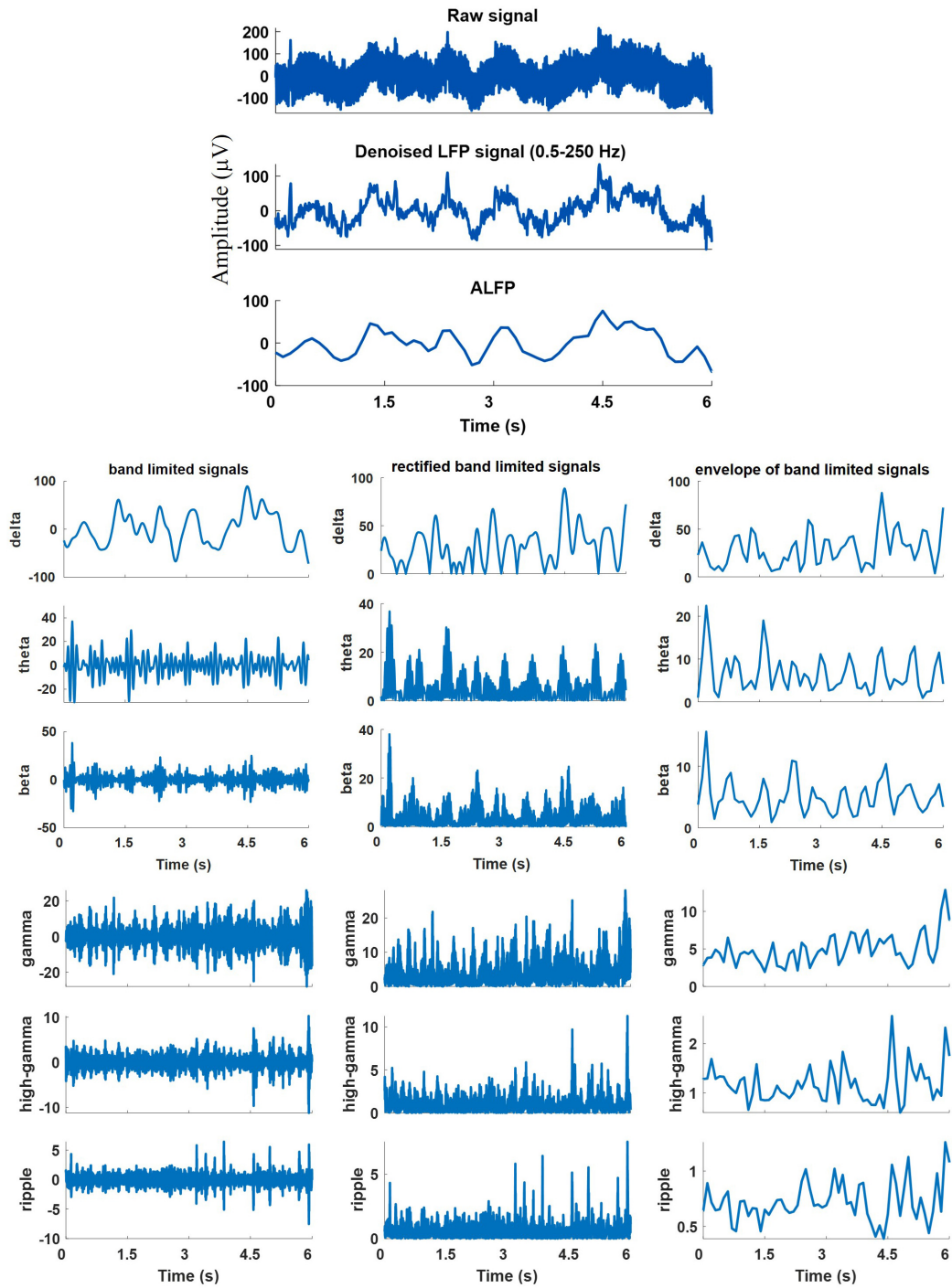
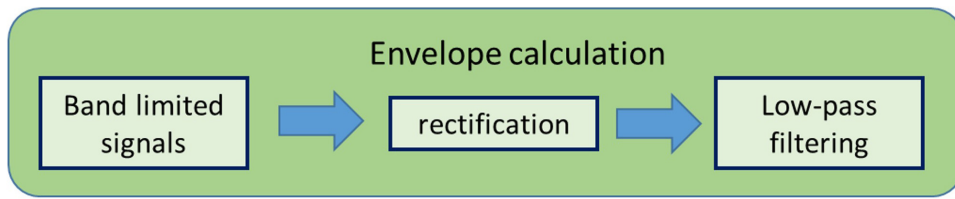
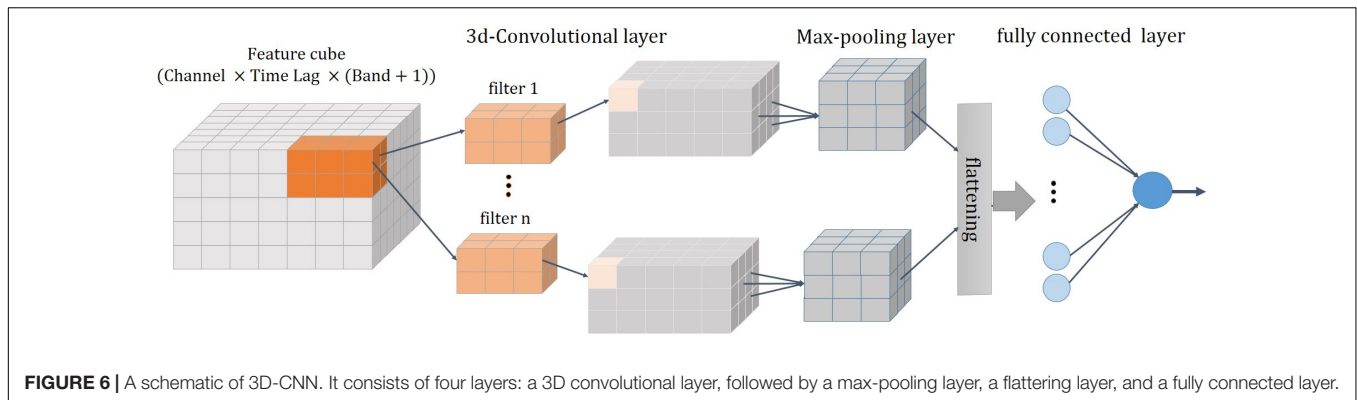
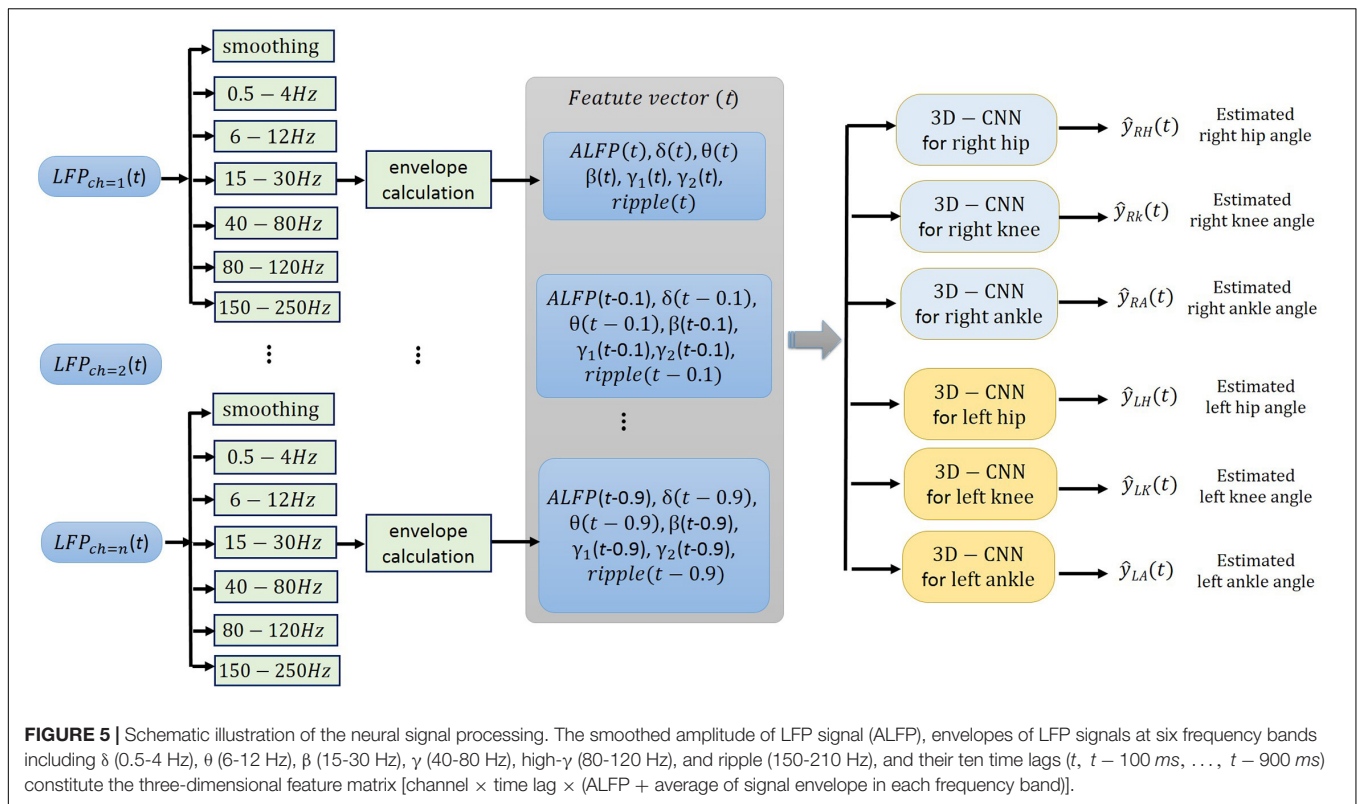


FIGURE 4 | An example of the recorded raw signal, corresponding extracted local field potential (LFP), extracted band-limited signals at different frequency bands, corresponding rectified signals, and their envelopes.

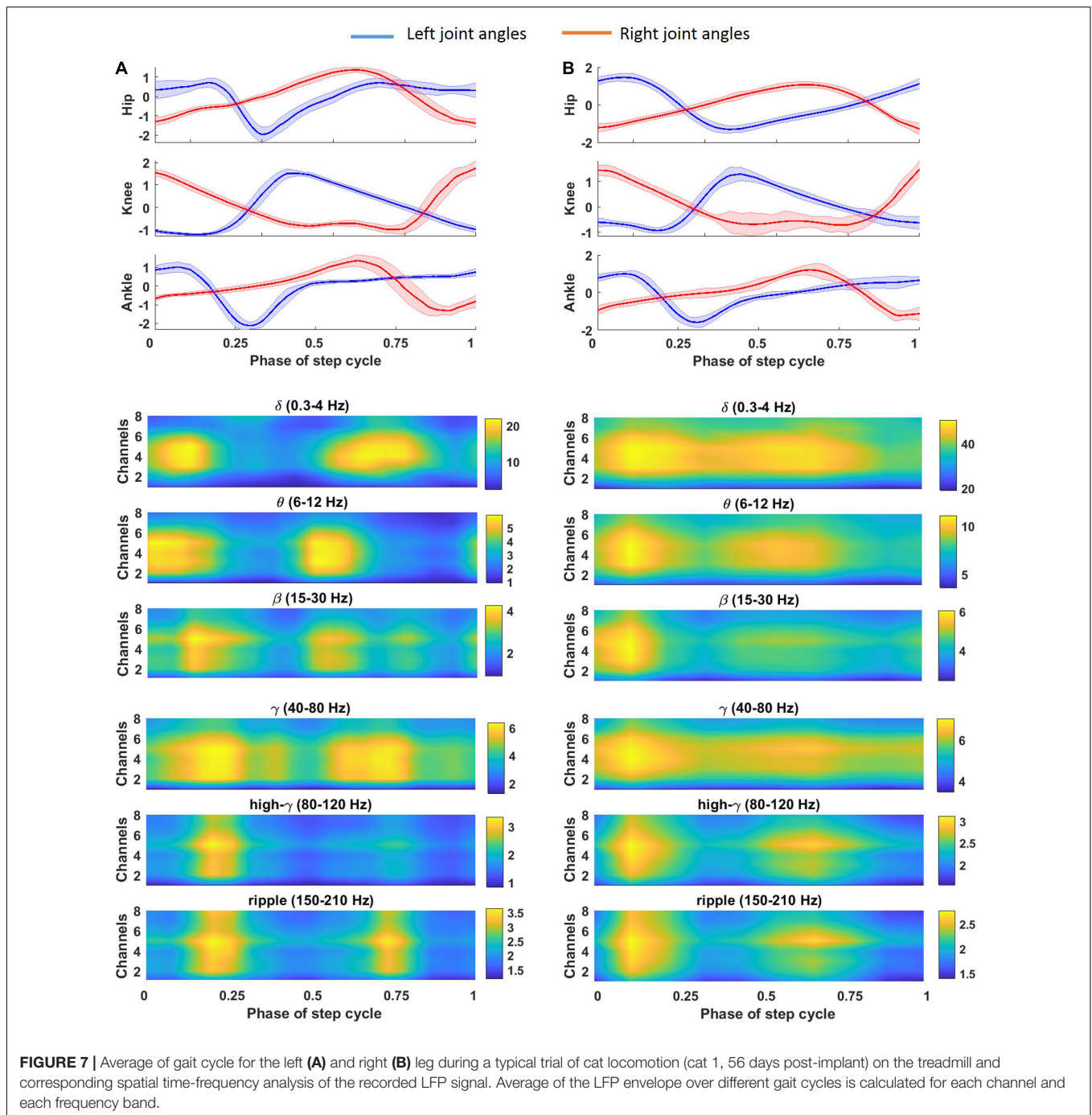


and displayed online using a custom-built LabVIEW program. **Figure 3** shows an example of the recorded joint angles from the left and right leg.

Neural Signals Recording and Preprocessing

The neural signals were measured using a multi-channel recording system (USB-ME64 system, Multichannel Systems Reutlingen, Germany) at a sampling rate of 500 Hz. Both the joint angles and the neural signals were synchronously captured using a custom-built LabVIEW (National Instruments, Austin, TX) program and saved for offline processing. Power line interference was removed using 4th order Butterworth notch filters at 50, 100, and 150 Hz. The signals were then band-pass

filtered into six frequency bands using 4th order Butterworth filters. The frequency bands consisted of δ (0.5-4 Hz), θ (6-12 Hz), β (15-30 Hz), γ (40-80 Hz), high- γ (80-120 Hz), and ripple (150-210 Hz). Then, the envelope of the signal at each frequency band was computed by low-pass filtering (4th order Butterworth with a cutoff frequency of 4 Hz) the rectified band-limited signal and then resampled at 10 Hz (**Figure 4**). In addition, the average amplitude of the local field potential (ALFP) signal was also calculated by taking the average of the LFP signal within sliding windows of 200-ms length and 100-ms step. Finally, ten time lags of the envelope of the signal at each frequency band and ten time lags of the average amplitude of the LFP signal at each time t (t , $t - 100$ ms, $t - 900$ ms) were used as the features for decoding the kinematics information (**Figure 5**). The feature space can be constituted

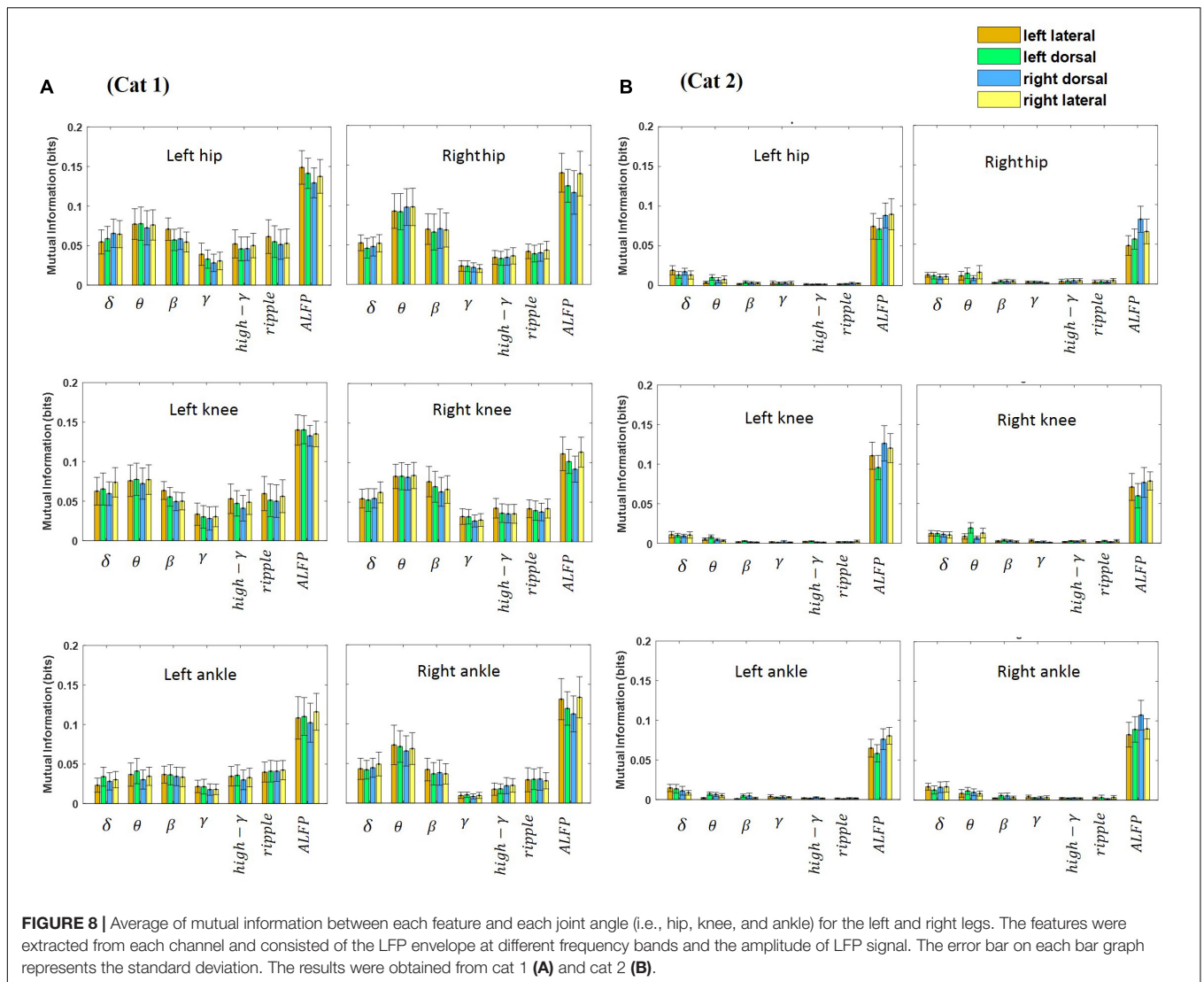


by a three-dimensional matrix (channel \times lag \times signal envelope at six frequency bands and ALFP features). This 3D feature matrix at each time was fed to the 3D-CNN to estimate the hindlimb joint angle.

Decoding Model

The architecture of the 3D-CNN proposed in this work for decoding is shown in **Figure 6**. It consists of four layers: a 3D convolutional layer, followed by a pooling layer, a fully connected layer, and a regression layer (Patterson and Gibson, 2017). The features described in the previous section were organized in a

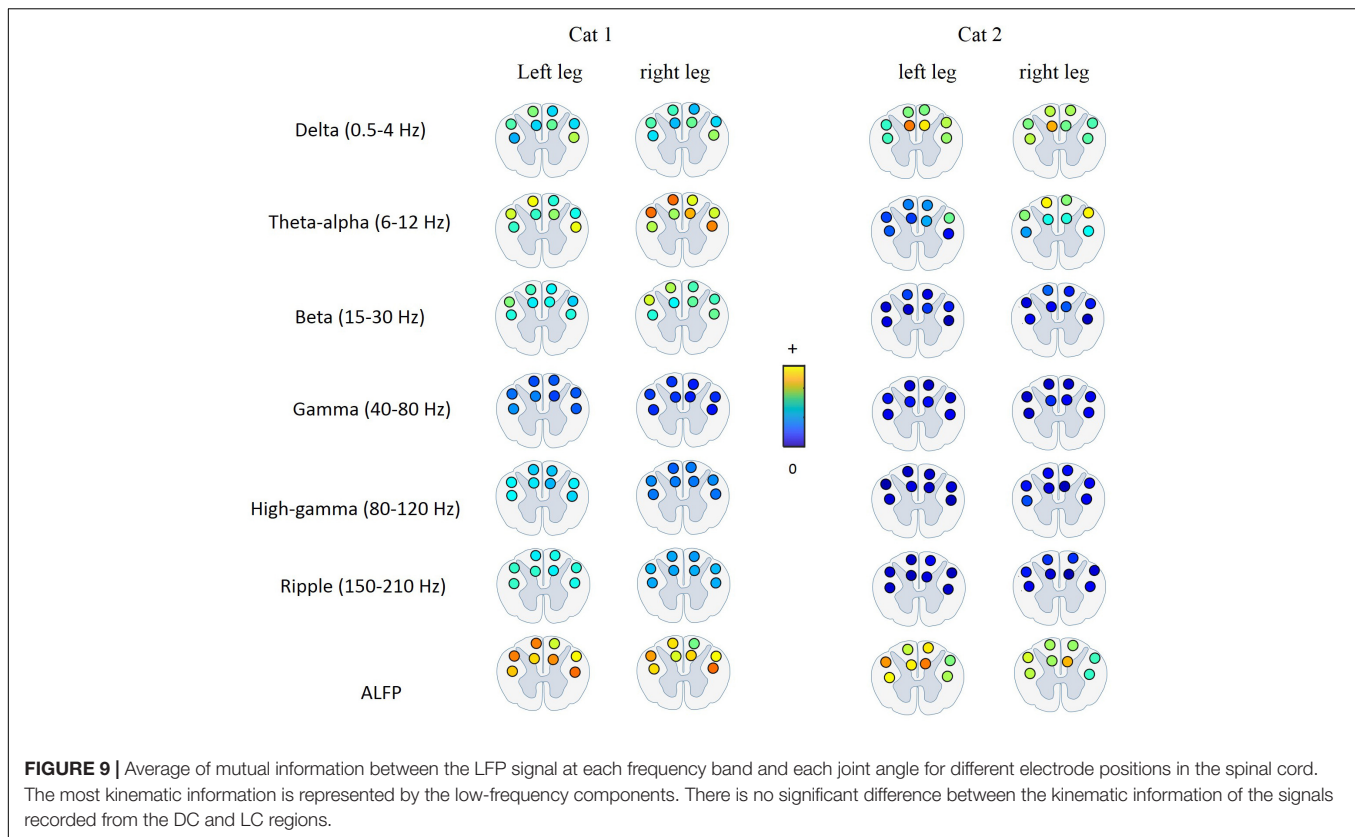
three-dimensional array [channel \times time lag \times (ALFP and average of signal envelope in each frequency band)] and then fed into the 3D convolutional layer. The convolution layer is the fundamental component of the CNN that uses the local correlation of the information in the input to extract features. The process of the convolution operation is convolving a filter (or a kernel) to the input and the result is a feature map (activation map). The filter is applied across the input volume in a sliding window manner. The filter out is computed at each position of the input by the dot product of the filter and the input window. This procedure is repeated with many different filters to form



different feature maps. Then, a nonlinear activation function is applied to the convolution-layer output. The rectified linear unit (ReLU) is considered as the activation function of the neurons in this layer. Two key parameters of the convolution operation are size and number of filters. In this study, a total of 70 filters of size $7 \times 6 \times 8$ are convolved into the input feature space with stride sizes of 1 in each dimension. The size of the filter and the number of filter are heuristically chosen to achieve the best classification performance. The distance that the window moves is called a stride. The common choice of a stride is 1. The convolutional layer followed by a pooling layer which reduces the dimensionality of the feature maps. The most common pooling operation is the max-pooling which extracts patches from the feature map and select the maximum value in each patch. Here, a max-pooling with a filter size of $2 \times 2 \times 2$ and a stride of 1 was used. The output of the pooling layer is flattened (i.e., transformed into a one-dimensional array) and connected to a fully connected layer. Here, fully connected layer is a single

hidden neural network with one output neuron. The output is the estimated joint angle.

Training a network is a process of estimating the weights of filters in convolution layer and weights in fully connected layers. The training is performed by minimizing a loss function which is of the mean squared error of estimation (differences between output predictions and measured values). The stochastic gradient descent with momentum solver is considered for minimizing the loss function and estimating the network. A regularization term for weights with a coefficient of 0.3 is also added to the loss function. The momentum that specifies the contribution of the last estimated parameter for the current parameter update is set to 0.75. Other training parameters, such as the mini-batch size and maximum number of epochs, are set to 128 and 10, respectively (Beale et al., 2017). These parameters are set based on the trial-and-error method and remained unchanged during the evaluation of all data.



Performance Evaluation

To assess the performance of the CNN in decoding the hindlimb kinematics, the coefficient of determination, R^2 value, was used. The R^2 can be defined as:

$$R^2 (\%) = \left(1 - \frac{\sum_{n=1}^N (y_n - \hat{y}_n)^2}{\sum_{n=1}^N (y_n - \bar{y})^2} \right) \times 100 \quad (1)$$

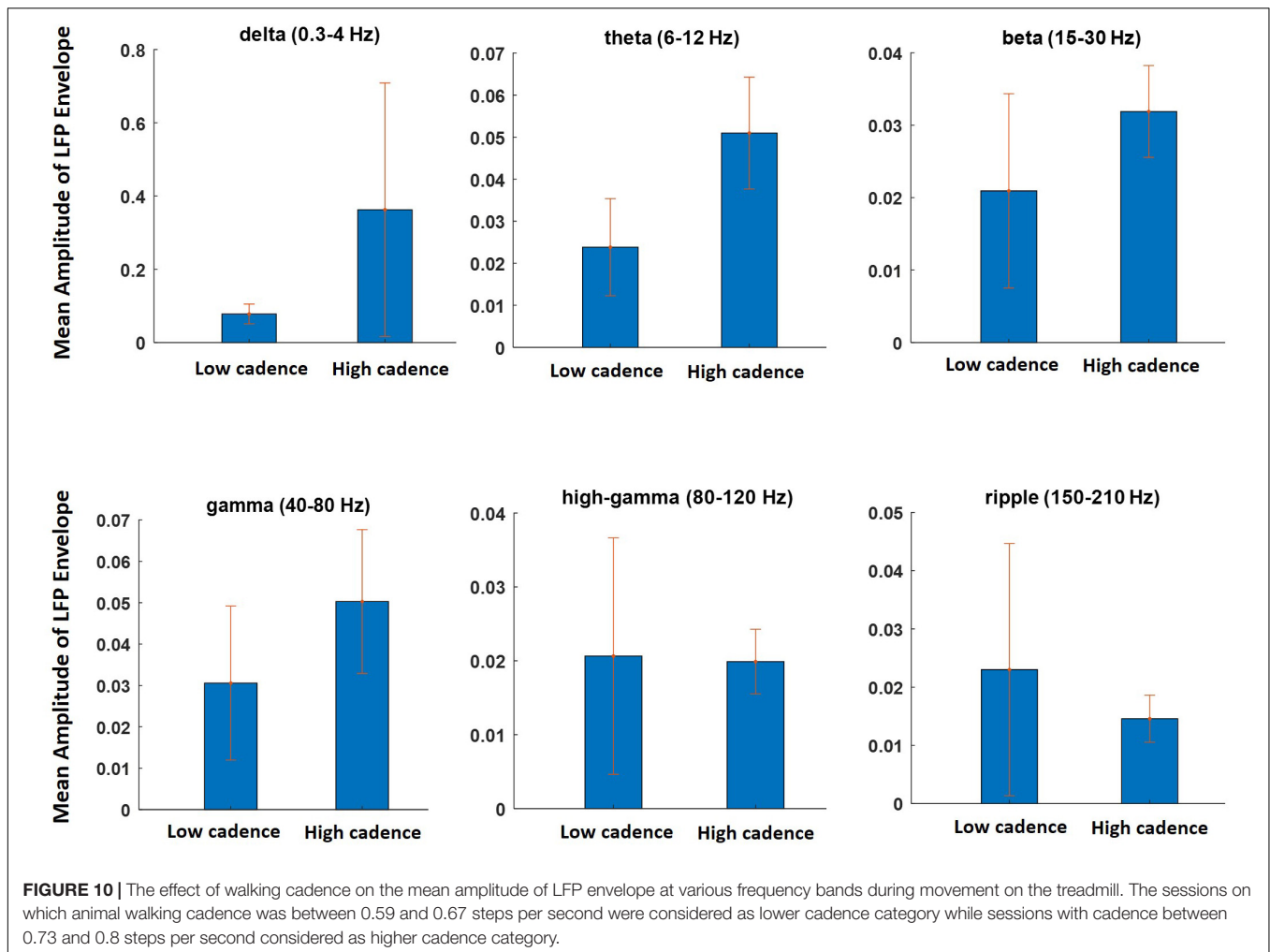
where y is the measured joint angle, \bar{y} is its mean value, \hat{y} is the estimated angle, and N is the number of data points. Threefold cross-validation was used to train and test the model using the data recorded during each session of the experiment. In threefold cross validation, the dataset was split into three equal parts (they are called folds). Two fold of the data (67%) obtained during each session of the experiment was assigned for training and the remaining fold (33% of the data) were assigned for testing the model. In the next round of threefold cross-validation, a different fold of data was selected for testing and the remaining folds for training. The average of decoding performance over the threefold and all the sessions of the experiment were reported. Moreover, mutual information (MI) was employed to evaluate the information content of the recorded neural signals. MI measures the mutual dependence of two or more variables. In other words, MI is a measure of the information that a random signal have on the other random signals and can be quantified using entropy. If two random variables are independent, then their mutual information is zero, but if the mutual information is large, it means two variables are closely related. Mutual

information was calculated based on an adaptive partitioning of the observation space (Darbellay and Vajda, 1999). MI has an advantage over the linear correlation coefficient in that it is able to capture both linear and nonlinear dependencies. MI was calculated between the extracted features from the LFP features at each frequency band and hindlimb kinematics. Analysis of variance (ANOVA) followed by Tukey's HSD post hoc test was used to assess the statistical significance of the results and differences. A confidence level of 95% ($p < 0.05$) was chosen to indicate a significant difference. All data analyses were performed with customized algorithms written in MATLAB.

RESULTS

Time-Frequency Analysis

The average of the gait cycle for the left and right legs during a typical trial of cat locomotion on the treadmill and the corresponding spatial time-frequency analysis of the recorded LFP signals are plotted in **Figure 7A**. It can be seen that a strong amplitude enhancement or event-related synchronization (ERS) and a strong amplitude attenuation or event-related desynchronization (ERD) occurred during joint flexion and extension, respectively. ERS and ERD occurred in both the dorsal column and lateral columns. ERS was observed in the ripple and high- γ bands during left hip flexion; β and γ bands during left ankle flexion; θ and β during left knee flexion; δ and β bands during right knee flexion; and δ and γ bands during right hip



and ankle flexion. A short ERS in the ripple band at 70% of the gait cycle can be associated with a small right knee flexion. **Figure 7B** shows the average of the time-frequency over all sessions of the experiment. Almost, the same ERS/ERD patterns were observed in the averaged time-frequency across all sessions but with broader distributed ERS pattern.

Mutual Information Analysis

The relative kinematic information of the LFP signal recorded from the lateral and dorsal columns during treadmill locomotion was investigated. Hence, MI was calculated between each joint angle and each band-limited LFP signal recorded from each electrode for all sessions of experiment (18 sessions for cat 1 and 10 sessions for cat 2) and then averaged over all sessions. All the data obtained during each session of experiment (from beginning of treadmill locomotion to termination) were used for calculating MI. Moreover, the MI between the ALFP and each joint angle was computed. **Figure 8** shows the average of the MI over the different sessions of the experiment and over the three joint angles at each frequency band for both legs and two cats. The results of the two-way ANOVA show that the ALFP contains significantly more information about limb kinematics than the frequency bands ($p < 10e-7$) in both cats. Comparing the information content of

the frequency bands, the results show that the θ band provides significantly more information than the other frequency bands ($p < 10e-7$) in cat 1, and the δ and θ bands were more informative than the other bands ($p < 0.01$) in cat 2. Moreover, it was found that the kinematics information of different spinal regions (i.e., left and right lateral columns, left and right dorsal columns) are not significantly different. Comparison between the information of channels in the left and right sides of the spinal cord showed that there was no significant difference between the two sides of the spinal cord, except for cat 2, where the ALFP at the right side of the spinal cord provides significantly greater MI for both legs ($p < 0.01$).

Figure 9 shows the average of MI between the LFP and hindlimb kinematics at different frequency bands for each recording channel and for both legs and both cats. It can be seen that the most kinematic information is represented by the low-frequency components. The results of the statistical test show that there is no significant difference between the kinematic information of the recording channels. This result is consistent with the previous study (Fathi and Erfanian, 2021) that the results show that there is no significant difference between the information content of the signals recorded from the DC and LC regions during walking on the treadmill.

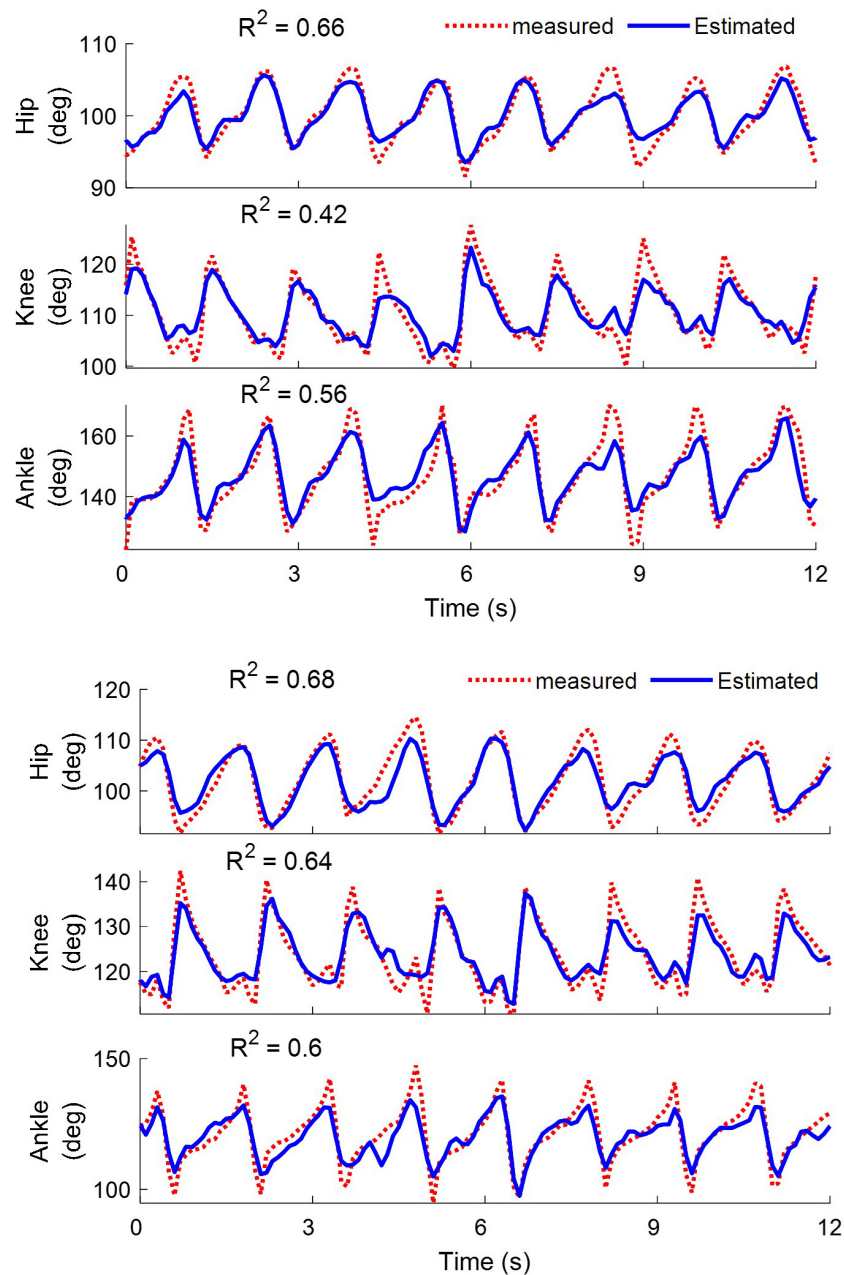


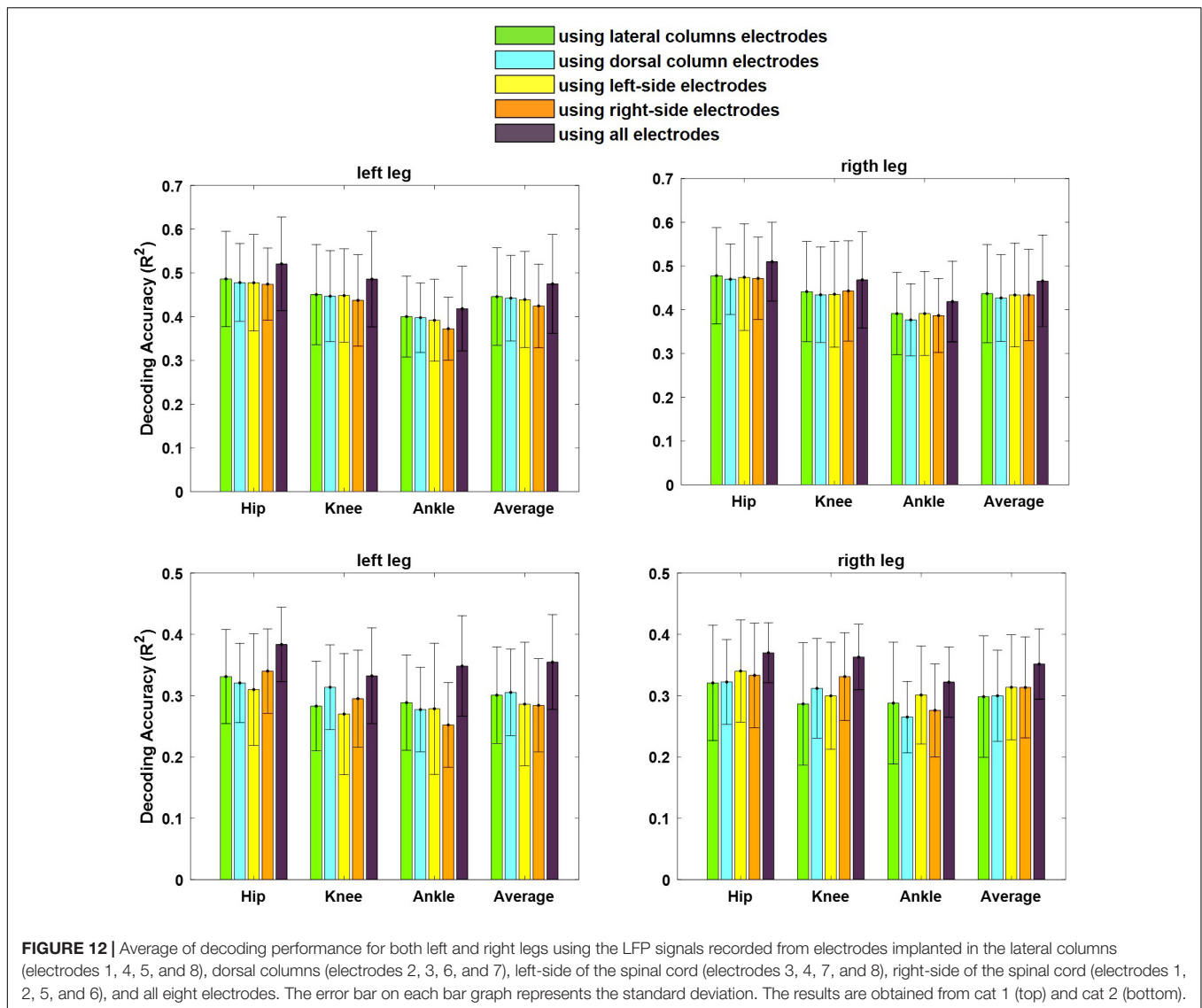
FIGURE 11 | Examples of decoding the hip, knee, and ankle joint angles for the left (**top**) and right leg (**bottom**) during walking on the treadmill. The results are obtained from cat 1 on day 12 after implantation. The coefficient of determination (R^2) values obtained for the left leg are 0.66, 0.42, and 0.56 for the hip, knee and ankle angles, respectively. For the right leg, the R^2 values are 0.68, 0.64, and 0.6 for the hip, knee, and ankle angles, respectively.

Effects of Walking Cadence

The effects of running speed on the oscillatory behavior of LFP signals recorded from the brain during locomotion have been investigated (Ahmed and Mehta, 2012; Bender et al., 2015; Noga et al., 2017). Increased running speed has been reported to be accompanied by hippocampal gamma oscillations (Ahmed and Mehta, 2012) and hippocampal theta oscillations (Bender et al., 2015). It was also demonstrated that theta LFP oscillations

in the mesencephalic locomotor region are correlated with the speed of locomotion (Noga et al., 2017).

In this section, the effects of the walking cadence on the LFP and the spectral features are investigated. The data from different sessions were divided into two subgroups: one with walking cadence lower than a lower threshold (0.67 steps per second) and the other with higher than the threshold (0.73 steps per second). The data obtained during 12 sessions of experiment



(6 sessions for low cadence and 6 sessions for high cadence) were selected for this analysis. We refer to these two groups as the lower and higher cadence groups, respectively. The mean envelope values of the LFP signals at different frequency bands were computed for both groups. **Figure 10** shows the results of the analysis. It can clearly be seen that the amplitude of the low-frequency components (i.e., delta, theta, beta, and gamma) increased during the high cadence of locomotion relative to that of the low cadence. However, this increase was not observed for the high-gamma and ripple components. The results of this analysis indicate that the LFP oscillations can reflect running speed. The results show that there is a significant difference between the mean amplitude of LFP envelope obtained during low cadence and high cadence walking only at the theta frequency band ($p = 0.03$).

Decoding and Its Performance

Figure 11 shows a typical example of decoding the joint angles in cat 1 while walking on the treadmill for the left

(top) and right (bottom) legs using the neural signals recorded from all electrodes implanted in the spinal cord. It can be seen that good tracking performance was obtained for all joints of two legs during hindlimb-only locomotion. The coefficients of determination (R^2) obtained for the hip, knee, and ankle joints of the left leg were 0.66, 0.42, and 0.56, respectively, and those for the right leg were 0.68, 0.64, and 0.60, respectively.

Figure 12 shows the average of the decoding performance for the left and right legs using the neural signals recorded from the left and right lateral columns (channels 1, 4, 5, and 8) as well as from the left and the right dorsal columns (channels 2, 3, 6, and 7) and from all channels. The results of the statistical analysis show that there is no significant difference ($p > 0.4$) between the performances obtained using the neural signals recorded from the lateral columns and that from the dorsal column for both cats. This result indicates that the lateral column can be used as the source of extracting motor information for motor neuroprosthesis.

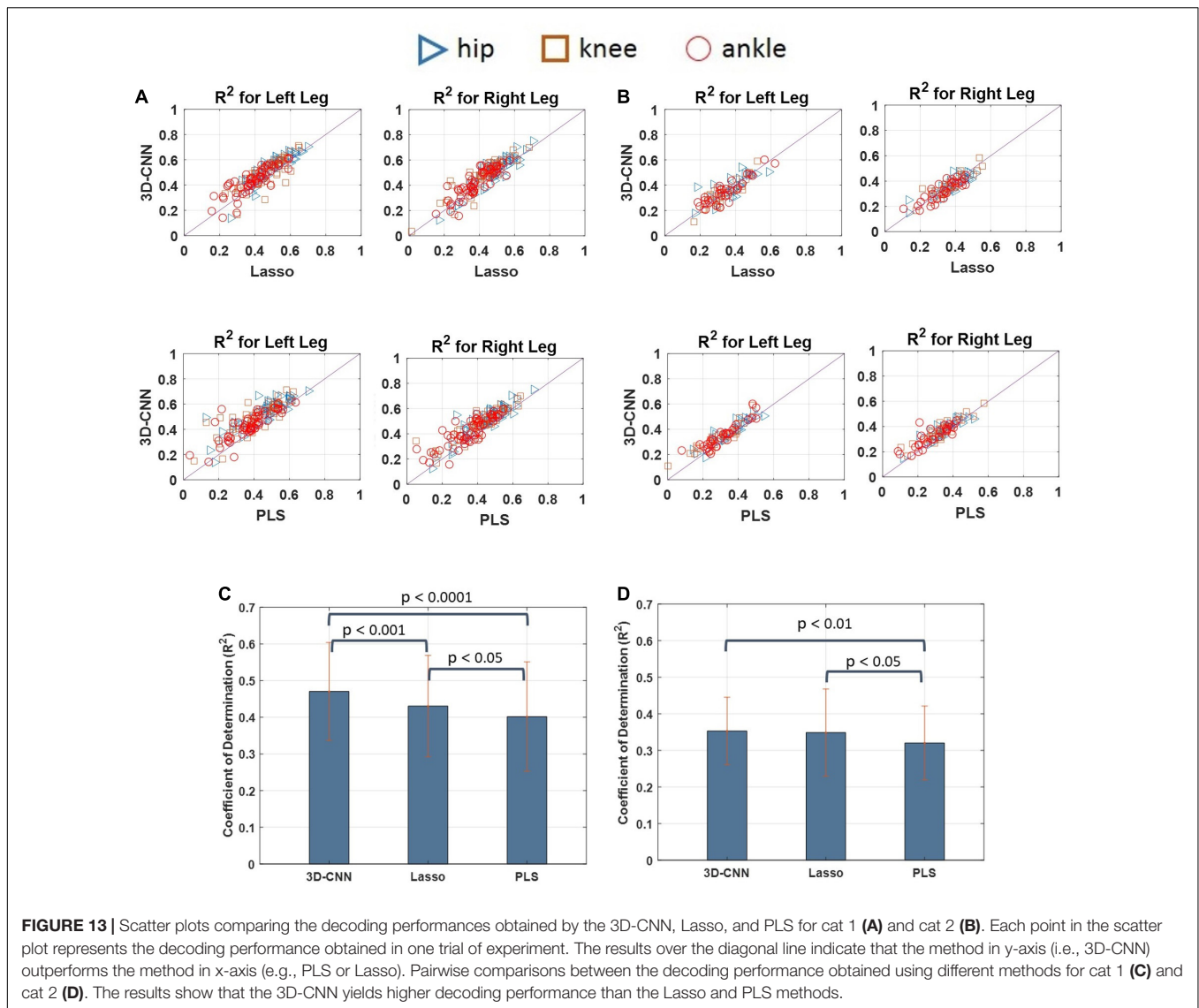


FIGURE 13 | Scatter plots comparing the decoding performances obtained by the 3D-CNN, Lasso, and PLS for cat 1 (A) and cat 2 (B). Each point in the scatter plot represents the decoding performance obtained in one trial of experiment. The results over the diagonal line indicate that the method in y-axis (i.e., 3D-CNN) outperforms the method in x-axis (e.g., PLS or Lasso). Pairwise comparisons between the decoding performance obtained using different methods for cat 1 (C) and cat 2 (D). The results show that the 3D-CNN yields higher decoding performance than the Lasso and PLS methods.

Furthermore, there was no significant difference between the decoding performance of the left and right legs using the neural signals recorded from the right side of the spinal cord ($p > 0.16$) (channels 1, 2, 5, and 6) as well as from the left side ($p > 0.27$) (channels 3, 4, 7, 8). Moreover, using all the channels in decoding could improve the decoding performance with $p < 0.05$ for cat 1 and with $p < 0.001$ for cat 2.

Decoding Model Comparison

The decoding performance of the 3D-CNN was also compared with that obtained using a conventional method such as the Lasso and PLS regression models. The decoding performance of the 3D-CNN was also compared with that obtained using a conventional method such as the Lasso and PLS regression models. The CNN was implemented using MATLAB with Deep Learning Toolbox and PLS as well as Lasso with Statistics and Machine Learning Toolbox. Pairwise comparisons of the decoding performance using scatterplots are provided in **Figures 13A,B** for cats 1 and 2, respectively. For cat 1, the decoding performance obtained

using the 3D-CNN model outperformed both the Lasso and PLS methods. For cat 2, it can be seen that the 3D-CNN outperformed the PLS, but no clear difference was observed when comparing the 3D-CNN with the Lasso method. **Figures 13C,D** show the average decoding performance over the left and right legs for each cat. One-way ANOVA with Tukey's HSD post hoc test was performed to compare the decoding performance using different methods. The results of statistical tests showed that the 3D-CNN outperformed the Lasso ($p < 0.001$) and PLS ($p < 0.0001$) in cat 1. In cat 2, the R^2 -values obtained using the 3D-CNN were significantly higher than those obtained using the PLS ($p < 0.01$), while no such difference exists between the 3D-CNN and Lasso.

DISCUSSION AND CONCLUSION

In this study, we explored the capability of descending and ascending spinal cord neural signals in decoding both

hindlimb kinematics. The decoding of the hindlimb kinematics information from the neural signals recorded from the descending tracts within the spinal cord indicates that the motor information could be extracted from these neural signals to develop motor neuroprostheses.

Here, we demonstrated that the neural signals recorded from the lateral columns can decode hindlimb kinematics as accurately as the dorsal columns. Interestingly, the neural signals from one side of the spinal cord could be used to decode both ipsilateral and contralateral hindlimb movements with very similar accuracy.

Decoding the ipsilateral and contralateral hindlimb movements indicates that the lateral columns contain information about the motor behaviors of discrete body parts. It has been reported that excitatory spinal interneurons are responsible for the timing and amplitude control of locomotor movements (Bouvier et al., 2015; Hayashi et al., 2018). Here, we showed that the lateral columns contain information about the timing and amplitude of the ipsilateral and contralateral movements. This finding suggests that supraspinal centers contribute to the locomotor coordination of timing and amplitude (Armstrong, 1986; Drew and Marigold, 2015; Frigon, 2017). In the current study, the results of the time-frequency analysis showed that the frequency bands of the LFP signals recorded from the lateral columns could represent the onset and offset of locomotor activity.

Although, the efferent signal carries motor information which is different from sensory information, the analysis of MI shows that there is no significant difference between hindlimb kinematics information obtained from the lateral columns and from the dorsal column during ipsilateral and contralateral movements. Interestingly, this result is in agreement with the results of decoding performance. The results of decoding show that there is no significant difference ($p > 0.4$) between the performances obtained using the neural signals recorded from the lateral columns and that from the dorsal column for both cats. Moreover, the MI analysis shows that the theta band provides significantly more information about the hindlimb kinematics than the other frequency bands ($p < 10e-7$). Previous studies have demonstrated that theta frequency oscillations of the hippocampal LFP are the main brain rhythm influenced by the periodic movements of locomotion (Ledberg and Robbe, 2011; Noga et al., 2017). Interestingly, our results also showed that the theta rhythm of the spinal LFP was associated with locomotor activity. It has also been shown that theta and gamma oscillations in the hippocampal increase in amplitude and frequency with faster running speed (Ledberg and Robbe, 2011; Ahmed and Mehta, 2012; Bender et al., 2015). Our primary results show that the power in different frequency bands changes with locomotion speed. In particular, the theta power increased with a higher locomotion speed. However, further experiments are required to provide further evidence.

Furthermore, we employed a state-of-the-art decoding model, 3D-CNN, to decode the hindlimb joint angles from the descending and ascending neural signals. The results show significant improvements in comparison to other well-known regression models in the field, such as the PLS and Lasso methods. However, the performance could still be increased by searching for optimal parameters or using deeper structures that

are beyond the scope of the current study and will be considered for future work.

In the current study, we used the LFPs of the ascending and descending tracts to decode the hindlimb kinematics during cat locomotion on the treadmill, whereas in the previous study (Fathi and Erfanian, 2019), spike activity recorded from the dorsal horn was used to decode the kinematics information during passive hindlimb movement. Here, we face an important unanswered question: which one of these spinal neural signals; LFPs or multi-unit spikes, is the most suitable for decoding hindlimb kinematics considering longevity of recording, movement artifact, and computational cost. Comparisons between the intracortical LFPs and multi-unit spikes have been performed by a number of groups (Jackson and Hall, 2017) and showed that LFPs were significantly more stable than spikes (Flint et al., 2016), however, since the spinal cord environment is tougher than the brain for recording, the intraspinal recording faces more severe challenges than intracortical recording and can be considered for future research purposes.

Furthermore, the results presented in the current study are based on the data obtained from two cats. To make broad conclusions, the experiments should be conducted on more cats which can be considered for future study.

DATA AVAILABILITY STATEMENT

The raw data supporting the conclusions of this article will be made available by the authors, without undue reservation.

ETHICS STATEMENT

The animals used in this study were kept and handled in compliance with the Experimental Animal Regulation Ordinances defined by the Ministry of Health and Medical Education, Iran. All surgical procedures and experimental protocols involving animal models described in this manuscript were approved by the Institutional Animal Care and Ethics Committee of the Iran Neural Technology Research Center, Iran University of Science and Technology. All protocols and methods were performed according to the recommendations and relevant guidelines for the care and use of laboratory animals.

AUTHOR CONTRIBUTIONS

AE and YF contributed to the design of experiments. YF conducted the experiments and analyzed the data. Both authors contributed to manuscript preparation and revision.

ACKNOWLEDGMENTS

We would like to thank Ali Roustazadeh for his assistance in preparing schematic figures of the spinal cord and microelectrode array. We would also like to thank Editage (www.editage.com) for English language editing.

REFERENCES

- Armstrong, D. M. (1986). Supraspinal contributions to the initiation and control of locomotion in the cat. *Prog. Neurobiol.* 26, 273–361. doi: 10.1016/0301-0082(86)90021-3
- Ahmed, O. J., and Mehta, M. R. (2012). Running speed alters the frequency of hippocampal gamma oscillations. *J. Neurosci.* 32, 7373–7383. doi: 10.1523/JNEUROSCI.5110-11.2012
- Barroso, F. O., Yoder, B., Tentler, D., Wallner, J. J., Kinkhabwala, A. A., Jantz, M. K., et al. (2019). Decoding neural activity to predict rat locomotion using intracortical and epidural arrays. *J. Neural Eng.* 16:36005. doi: 10.1088/1741-2552/ab0698
- Beale, M. H., Hagan, M. T., and Demuth, H. B. (2017). *MATLAB Neural Network Toolbox User's Guide (version R2017b)*. Natick, MA: MathWorks.
- Bender, F., Gorbati, M., Cadavieco, M. C., Denisova, N., Gao, X., Holman, C., et al. (2015). Theta oscillations regulate the speed of locomotion via a hippocampus to lateral septum pathway. *Nat. Commun.* 6:8521. doi: 10.1038/ncomms9521
- Bonizzato, M., Pidpruzhnykova, G., DiGiovanna, J., Shkorbatova, P., Pavlova, N., Micera, S., et al. (2018). Brain-controlled modulation of spinal circuits improves recovery from spinal cord injury. *Nat. Commun.* 9:3015. doi: 10.1038/s41467-018-05282-6
- Bouvier, J., Caggiano, V., Leiras, R., Caldeira, V., Bellardita, C., Balueva, K., et al. (2015). Descending command neurons in the brainstem that halt locomotion. *Cell* 163, 1191–1203. doi: 10.1016/j.cell.2015.10.074
- Bruns, T. M., Wagenaar, J. B., Bauman, M. J., Gaunt, R. A., and Weber, D. J. (2013). Real-time control of hind limb functional electrical stimulation using feedback from dorsal root ganglia recordings. *J. Neural Eng.* 10:026020. doi: 10.1088/1741-2560/10/2/026020
- Capogrosso, M., Milekovic, T., Borton, D., Wagner, F., Moraud, E. M., Mignardot, J.-B., et al. (2016). A brain–spine interface alleviating gait deficits after spinal cord injury in primates. *Nature* 539, 284–288. doi: 10.1038/nature20118
- Craik, A., He, Y., and Contreras-Vidal, J. L. (2019). Deep learning for electroencephalogram (EEG) classification tasks: a review. *J. Neural Eng.* 16:31001. doi: 10.1088/1741-2552/ab0ab5
- Darbellay, G. A., and Vajda, I. (1999). Estimation of the information by an adaptive partitioning of the observation space. *IEEE Trans. Inf. Theory* 45, 1315–1321. doi: 10.1109/18.761290
- Debnath, S., Bauman, M. J., Fisher, L. E., Weber, D. J., and Gaunt, R. A. (2014). Microelectrode array recordings from the ventral roots in chronically implanted cats. *Front. Neurol.* 5:104. doi: 10.3389/fneur.2014.00104
- Drew, T., and Marigold, D. S. (2015). Taking the next step: cortical contributions to the control of locomotion. *Curr. Opin. Neurobiol.* 33, 25–33. doi: 10.1016/j.conb.2015.01.011
- Fathi, Y., and Erfanian, A. (2019). A probabilistic recurrent neural network for decoding hind limb kinematics from multi-segment recordings of the dorsal horn neurons. *J. Neural Eng.* 16:036023. doi: 10.1088/1741-2552/ab0e51
- Fathi, Y., and Erfanian, A. (2021). Decoding hindlimb kinematics from descending and ascending neural signals during cat locomotion. *J. Neural Eng.* 18:26015. doi: 10.1088/1741-2552/abd82a
- Flint, R. D., Scheid, M. R., Wright, Z. A., Solla, S. A., and Slutzky, M. W. (2016). Long-term stability of motor cortical activity: implications for brain machine interfaces and optimal feedback control. *J. Neurosci.* 36, 3623–3632. doi: 10.1523/JNEUROSCI.2339-15.2016
- Fitzsimmons, N., Lebedev, M., Peikon, I., and Nicolelis, M. (2009). Extracting kinematic parameters for monkey bipedal walking from cortical neuronal ensemble activity. *Front. Integr. Neurosci.* 3:3. doi: 10.3389/fnint.2009.07.03.2009
- Frigon, A. (2017). The neural control of interlimb coordination during mammalian locomotion. *J. Neurophysiol.* 117, 2224–2241. doi: 10.1152/jn.00978.2016
- Frigon, A., Rossignol, S., and Frigon, A. (2011). Recovery of locomotion after spinal cord injury?: some facts and mechanisms. *Annu. Rev. Neurosci.* 34, 413–440. doi: 10.1146/annurev-neuro-061010-113746
- Gao, Y., Gao, B., Chen, Q., Liu, J., and Zhang, Y. (2020). Deep convolutional neural network-based epileptic electroencephalogram (EEG) signal classification. *Front. Neurol.* 11:375. doi: 10.3389/fneur.2020.00375
- Geladi, P., and Kowalski, B. (1986). Partial least-squares regression: a tutorial. *Anal. Chim. Acta* 185, 1–17. doi: 10.1016/0003-2670(86)80028-9
- Gok, S., and Sahin, M. (2019). Prediction of forelimb EMGs and movement phases from corticospinal signals in the rat during the reach-to-pull task. *Int. J. Neural Syst.* 29:1950009. doi: 10.1142/S0129065719500096
- Guo, Y., Foulds, R. A., Adamovich, S. V., and Sahin, M. (2014). Encoding of forelimb forces by corticospinal tract activity in the rat. *Front. Neurosci.* 8:62. doi: 10.3389/fnins.2014.00062
- Guo, Y., Gok, S., and Sahin, M. (2018). Convolutional networks outperform linear decoders in predicting EMG from spinal cord signals. *Front. Neurosci.* 12:689. doi: 10.3389/fnins.2018.00689
- Han, S., Chu, J. U., Kim, H., Park, J. W., and Youn, I. (2017). Multiunit activity-based real-time limb-state estimation from dorsal root ganglion recordings. *Sci. Rep.* 7, 1–14. doi: 10.1038/srep44197
- Hansen, M., Haugland, M. K., and Sinkjær, T. (2004). Evaluating robustness of gait event detection based on machine learning and natural sensors. *IEEE Trans. Neural Syst. Rehabil. Eng.* 12, 81–88. doi: 10.1109/TNSRE.2003.819890
- Harnie, J., Audet, J., Mari, S., Lecomte, C. G., Merlet, A. N., Genois, G., et al. (2022). State-and condition-dependent modulation of the hindlimb locomotor pattern in intact and spinal cats across speeds. *Front. Syst. Neurosci.* 16:814028. doi: 10.3389/fnsys.2022.814028
- Hayashi, M., Hinkley, C. A., Driscoll, S. P., Moore, N. J., Levine, A. J., Hilde, K. L., et al. (2018). Graded arrays of spinal and supraspinal V2a interneuron subtypes underlie forelimb and hindlimb motor control. *Neuron* 97, 869.e–884.e. doi: 10.1016/j.neuron.2018.01.023
- Holinski, B. J., Everaert, D. G., Mushahwar, V. K., and Stein, R. B. (2013). Real-time control of walking using recordings from dorsal root ganglia. *J. Neural Eng.* 10:056008. doi: 10.1088/1741-2560/10/5/056008
- Jackson, A., and Zimmermann, J. B. (2012). Neural interfaces for the brain and spinal cord—restoring motor function. *Nat. Rev. Neurol.* 8, 690–699. doi: 10.1038/nrneuro.2012.219
- Jackson, A., and Hall, T. M. (2017). Decoding local field potentials for neural interfaces. *IEEE Trans. Neural Syst. Rehabil. Eng.* 25, 1705–1714. doi: 10.1109/TNSRE.2016.2612001
- Kashkoush, A. I., Gaunt, R. A., and Weber, D. J. (2019). Recording single- and multi-unit neuronal action potentials from the surface of the dorsal root ganglion. *Sci. Rep.* 9, 1–12. doi: 10.1038/s41598-019-38924-w
- Knudsen, E. B., and Moxon, K. A. (2017). Restoration of hindlimb movements after complete spinal cord injury using brain-controlled functional electrical stimulation. *Front. Neurosci.* 11:715. doi: 10.3389/fnins.2017.00715
- Kundu, S., and Ari, S. (2020). MsCNN: a deep learning framework for P300-based brain-computer interface speller. *IEEE Trans. Med. Robot. Bionics* 2, 86–93. doi: 10.1109/TMRB.2019.2959559
- Lawhern, V. J., Solon, A. J., Waytowich, N. R., Gordon, S. M., Hung, C. P., and Lance, B. J. (2018). EEGNet: a compact convolutional neural network for EEG-based brain-computer interfaces. *J. Neural Eng.* 15:056013. doi: 10.1088/1741-2552/aace8c
- LeCun, Y., Bengio, Y., and Hinton, G. (2015). Deep learning. *Nature* 521, 436–444. doi: 10.1038/nature14539
- Ledberg, A., and Robbe, D. (2011). Locomotion-related oscillatory body movements at 6–12 Hz modulate the hippocampal theta rhythm. *PLoS One* 6:e27575. doi: 10.1371/journal.pone.0027575
- Lemon, R. N. (2008). Descending pathways in motor control. *Annu. Rev. Neurosci.* 31, 195–218. doi: 10.1146/annurev-neuro.31.060407.125547
- Li, W., Zhu, L., Shi, Y., Guo, K., and Cambria, E. (2020). User reviews: sentiment analysis using lexicon integrated two-channel CNN–LSTM family models. *Appl. Soft Comput.* 94:106435. doi: 10.1016/j.asoc.2020.106435
- Li, Y., Zhao, J., Lv, Z., and Pan, Z. (2021). Multimodal medical supervised image fusion method by CNN. *Front. Neurosci.* 15:303. doi: 10.3389/fnins.2021.638976
- Liu, D., Li, Y., Lin, J., Li, H., and Wu, F. (2020). Deep learning-based video coding: a review and a case study. *ACM Comput. Surv.* 53:11. doi: 10.1145/3368405
- Micera, S., Jensen, W., Sepulveda, F., Riso, R. R., and Sinkjær, T. (2001). Neuro-fuzzy extraction of angular information from muscle afferents for ankle control during standing in paraplegic subjects: an animal model. *IEEE Trans. Biomed. Eng.* 48, 787–794. doi: 10.1109/10.930903
- Mustaqeem, and Kwon, S. (2020). A CNN-assisted enhanced audio signal processing for speech emotion recognition. *Sensors* 20:183. doi: 10.3390/s20010183

- Noga, B. R., Sanchez, F. J., Villamil, L. M., O'Toole, C., Kasicki, S., Olszewski, M., et al. (2017). LFP oscillations in the mesencephalic locomotor region during voluntary locomotion. *Front. Neural Circuits* 11:34. doi: 10.3389/fncir.2017.00034
- Patterson, J., and Gibson, A. (2017). *Deep Learning: A Practitioner's Approach*. Sebastopol, CA: O'Reilly Media, Inc.
- Petrosyan, A., Sinkin, M., Lebedev, M., and Ossadtchi, A. (2021). Decoding and interpreting cortical signals with a compact convolutional neural network. *J. Neural Eng.* 18:026019. doi: 10.1088/1741-2552/abe20e
- Prasad, A., and Sahin, M. (2006). Extraction of motor activity from the cervical spinal cord of behaving rats. *J. Neural Eng.* 3, 287–292. doi: 10.1088/1741-2560/3/4/005
- Prasad, A., and Sahin, M. (2010). Characterization of neural activity recorded from the descending tracts of the rat spinal cord. *Front. Neurosci.* 4:21. doi: 10.3389/fnins.2010.00021
- Prasad, A., and Sahin, M. (2012). Can motor volition be extracted from the spinal cord? *J. Neuroeng. Rehabil.* 9:41. doi: 10.1186/1743-0003-9-41
- Rigosa, J., Panarese, A., Dominici, N., Friedli, L., van den Brand, R., Carpaneto, J., et al. (2015). Decoding bipedal locomotion from the rat sensorimotor cortex. *J. Neural Eng.* 12:56014. doi: 10.1088/1741-2560/12/5/056014
- Rigosa, J., Weber, D. J., Prochazka, A., Stein, R. B., and Micera, S. (2011). Neuro-fuzzy decoding of sensory information from ensembles of simultaneously recorded dorsal root ganglion neurons for functional electrical stimulation applications. *J. Neural Eng.* 8:046019. doi: 10.1088/1741-2560/8/4/046019
- Riso, R. R., Mosallaei, F. K., Jensen, W., and Sinkjaer, T. (2000). Nerve cuff recordings of muscle afferent activity from tibial and peroneal nerves in rabbit during passive ankle motion. *IEEE Trans. Rehabil. Eng.* 8, 244–258. doi: 10.1152/physiol.00042.2008
- Rosignol, S., Barrière, G., Alluin, O., and Frigon, A. (2009). Re-expression of locomotor function after partial spinal cord injury. *Physiology* 24, 127–139. doi: 10.1152/physiol.00042.2008
- Song, I., Chu, J. U., Park, S. E., Hwang, D., and Youn, I. (2017). Ankle-angle estimation from blind source separated afferent activity in the sciatic nerve for closed-loop functional neuromuscular stimulation system. *IEEE Trans. Biomed. Eng.* 64, 834–843. doi: 10.1109/TBME.2016.2580705
- Song, W., Ramakrishnan, A., Udoekwere, U. I., and Giszter, S. F. (2009). Multiple types of movement-related information encoded in hindlimb/trunk cortex in rats and potentially available for brain-machine interface controls. *IEEE Trans. Biomed. Eng.* 56, 2712–2716. doi: 10.1109/TBME.2009.2026284
- Stein, R. B., Weber, D. J., Aoyagi, Y., Prochazka, A., Wagenaar, J. B. M., Shoham, S., et al. (2004). Coding of position by simultaneously recorded sensory neurones in the cat dorsal root ganglion. *J. Physiol.* 560, 883–896. doi: 10.1113/jphysiol.2004.068668
- Takakusaki, K., Chiba, R., Nozu, T., and Okumura, T. (2016). Brainstem control of locomotion and muscle tone with special reference to the role of the mesopontine tegmentum and medullary reticulospinal systems. *J. Neural Transm.* 123, 695–729. doi: 10.1007/s00702-015-1475-4
- Wagenaar, J. B., Ventura, V., and Weber, D. J. (2011). State-space decoding of primary afferent neuron firing rates. *J. Neural Eng.* 8:016002. doi: 10.1088/1741-2560/8/1/016002
- Weber, D. J., Stein, R. B., Everaert, D. G., and Prochazka, A. (2006). Decoding sensory feedback from firing rates of afferent ensembles recorded in cat dorsal root ganglia in normal locomotion. *IEEE Trans. Neural Syst. Rehabil. Eng.* 14, 240–243. doi: 10.1109/TNSRE.2006.875575
- Weber, D. J., Stein, R. B., Everaert, D. G., and Prochazka, A. (2007). Limb-state feedback from ensembles of simultaneously recorded dorsal root ganglion neurons. *J. Neural Eng.* 4, S168–S180. doi: 10.1088/1741-2560/4/3/S04
- Widiastuti, N. I. (2019). Convolution neural network for text mining and natural language processing. *IOP Conf. Ser. Mater. Sci. Eng.* 662:52010. doi: 10.1088/1757-899x/662/5/052010
- Xie, Z., Schwartz, O., and Prasad, A. (2018). Decoding of finger trajectory from ECoG using deep learning. *J. Neural Eng.* 15:36009. doi: 10.1088/1741-2552/aa9dbe
- Yeganegi, H., Fathi, Y., and Erfanian, A. (2018). Decoding hind limb kinematics from neuronal activity of the dorsal horn neurons using multiple level learning algorithm. *Sci. Rep.* 8:577. doi: 10.1038/s41598-017-18971-x
- Zhang, X., Yao, L., Wang, X., Monaghan, J., McAlpine, D., and Zhang, Y. (2021). A survey on deep learning-based non-invasive brain signals: recent advances and new frontiers. *J. Neural Eng.* 18:31002. doi: 10.1088/1741-2552/abc902
- Zou, H., and Hastie, T. (2005). Regularization and variable selection via the elastic net. *J. R. Stat. Soc. Ser. B* 67, 301–320. doi: 10.1111/j.1467-9868.2005.00503.x

Conflict of Interest: The authors declare that the research was conducted in the absence of any commercial or financial relationships that could be construed as a potential conflict of interest.

Publisher's Note: All claims expressed in this article are solely those of the authors and do not necessarily represent those of their affiliated organizations, or those of the publisher, the editors and the reviewers. Any product that may be evaluated in this article, or claim that may be made by its manufacturer, is not guaranteed or endorsed by the publisher.

Copyright © 2022 Fathi and Erfanian. This is an open-access article distributed under the terms of the Creative Commons Attribution License (CC BY). The use, distribution or reproduction in other forums is permitted, provided the original author(s) and the copyright owner(s) are credited and that the original publication in this journal is cited, in accordance with accepted academic practice. No use, distribution or reproduction is permitted which does not comply with these terms.